Microstructure Evolution and Anisotropy Effect During Low Temperature Cross Rolling and Annealing of Ti6Al4V

WEN-GUANG ZHU, JIAO PU, CONG-HUI ZHANG, QIN-BO WANG, YI-LEI WANG, TING-CHUAN SHU, XIAO-XIANG WANG, and JIAN WANG

In order to obtain ultrafine isotropic titanium alloy plate, β phase quenching and the subsequent low temperature α/β phase cross rolling are employed in this paper. The microstructure evolution, texture variation and recrystallization behavior are characterized by scanning electron microscope (SEM) and electron back-scattered diffraction (EBSD). Tensile properties of the as cross rolled and annealed plates were investigated. The microstructure dependences of strength difference in TD and RD samples were discussed in detail. The results suggest that discontinuous dynamic recrystallization (DDRX) takes place incompletely which results in a refined but inhomogeneous microstructure after first cross rolling. After second cross rolling, a refined grain with average size ~ 1.24 μm is obtained. The texture is transformed into a B-type ([0001]//ND) texture which results in limited strength differences between TD and RD sample. During subsequent annealing treatment, continuous static recrystallization (CSRX) generates an equiaxed uniform microstructure and the grain size increases with increasing annealing temperature. Tensile tests suggest that TD samples exhibit a higher strength than that of the RD sample in both cross rolling and annealing condition. The strength difference is decreasing with increasing annealing temperature. Finally, the Schmid law is used to analyze the strength difference in TD and RD direction. The RD sample displayed highest SF value for prismatic and pyramidal $\langle a \rangle$ slip system which is the origin of the lower yield strength. With increasing annealing temperature, SF value difference of prismatic $\langle a \rangle$ slip system between RD and TD sample is decreasing which is beneficial to reduce anisotropy of Ti6Al4V plates.

I. INTRODUCTION

ULTRA-FINE grained (UFG) titanium alloy exhibits excellent mechanical properties, such as improved strength-ductility combination and superior superplasticity forming capacity.[1–5] The physical metallurgy-based grain refining techniques are mainly severe plastic deformation (SPD) and thermomechanical processes (TMP). SPD process such as high-pressure torsion (HPT), equal-channel angular pressing (ECAP), accumulative roll bonding (ARB), multiaxial forging (MAF), twisted variable channel angular pressing (TV-CAP) multi-angular twist channel extrusion (MATE), indirect Extrusion Angular Pressing (IEAP) and forging-bending repeated deformation process could produce nanocrystals in titanium and titanium alloys.[6–16] However, it is difficult to create large-size products efficiently and steadily. There are still only a few industrial applications that are really applicable.

Thermomechanical processing (TMP) is an effective method for the industrial preparation of ultra-fine grains.[17] The process is widely used in steel materials, especially the austenitic-ferritic two-phase region TMP process, which combines the effects of both plastic deformation and phase transformation, facilitating the dynamic phase transformation and dynamic recrystallization (DRX) simultaneously, resulting in remarkable refinement.[18] An ultra-fine A/F structure is generated in medium manganese steels using dual-phase warm rolling and microalloying of V.[19] Wang[20] found that

WEN-GUANG ZHU is with the School of Metallurgical Engineering, Xi'an University of Architecture and Technology, Xi'an 710055, P.R. China and also with the BAOTI Group Co., Ltd, No.88, High Tech Road, Baoji 721014, Shaanxi, P.R. China. JIAO PU, CONG-HUI ZHANG, and TING-CHUAN SHU are with the School of Metallurgical Engineering, Xi'an University of Architecture and Technology. Contact e-mail: zhangconghui@xauat.edu.cn QIN-BO WANG, XIAO-XIANG WANG, and JIAN WANG are with the BAOTI Group Co., Ltd. YI-LEI WANG is with the State Key Laboratory of Solidification Processing, Northwestern Polytechnical University, Xi'an 710072, Shaanxi, P.R. China.

by A/F two-phase rolling (750 °C–810 °C) and intercritical quenching, the original ferrite grain could be refined to 1.47–1.98 μm, which facilitates the alloy exhibits excellent strength and ductility combination. Inoue[21] used warm bi-axial rolling with total reduction of 88 pct at 550 °C to successfully generate 1.2 μm ferrite grains in 0.15 pctC-0.3 pctSi-1.5 pctMn low carbon steel. Hu[22] prepared 0.3–0.4 μm ultra-fine grains in low-alloyed low carbon steels by ferrite/martensite deformation during which both dynamic phase transformation, intergranular nucleation and DRX takes place.

However, the study on TMP process for titanium alloy grain refinement is relatively limited which is mainly at the laboratory stage. Semiatin[23] suggested that an ultra-fine Ti6Al4V grain could obtained by rolling at the α/β two-phase region at which sufficient recrystallization of the α-phase and suppression of grain growth is detected. More researches have focused on the microstructure evolution and recrystallization mechanism of titanium alloy in α/β two-phase region using Gleeble thermal mechanical simulator. Liang[24] suggested that dynamic recovery (DRV) and DRX are competitive with each other. DRV happens at high strain rates and low temperatures, while DRX is usually observed at low strain rates and high temperatures. The research in TA15[25] found that the DRX mechanism depends on the deformation temperature, continuous DRX (CDRX) dominating at low deformation temperatures (750 °C) and discontinuous DRX (DDRX) dominating at high temperatures (> 850 °C). Wang[26] pointed out that CDRX is the dominate recrystallization mechanism in TC21 alloy when deformed at 820 °C–860 °C, and CDRX is suppressed by increasing deformation temperature. Chiba[27] found that the thermal deformation mechanism is related to the initial microstructure and thickness reductions. DDRX occurs in lamellar structure while CDRX occurs in equiaxed structure. In general, the deformation process in the α/β two-phase region involves $\beta \rightarrow \alpha$ phase transformation, DRX, interaction between α and β phase. The microstructure evolution depending on alloy composition, initial microstructure type, deformation temperature, plastic reductions, strain rates. Moreover, the existing study were mainly performed on Gleeble simulation machine with 8×12 mm cylinder sample which is very different from hot rolling process. Thus, it is essential to study on the microstructure evolution and DRX mechanism of titanium alloy during rolling process, particularly during cross rolling in the two-phase region.

During hot rolling of duplex titanium alloys, the T-type texture of [0001]//TD or the B ([0001]//ND) + T-type texture was usually formed.[28] The T-type texture results in a higher transverse strength than the longitudinal one, which generates a rough, orange peel surface after superplastic forming.[29] Cross rolling is an important method to modify the type and intensity of texture. The study of Hu,[30] Catorceno et al.[31] in AZ31 and RE-Mg alloys found that cross rolling considerably weakened the B-type texture and reduced the alloy anisotropy. The study in 7075[32] aluminum alloy

showed that the brass and cubic texture intensity were significantly reduced and the S and Dillamore textures disappeared after the cross rolling and annealing. In titanium alloys, the effect of cross rolling on the intensity and type of texture is related to deformation temperature, reduction degree before and after cross rolling.[33,34] Zhiyong Chen studied the cross rolling of Ti-60 alloy in the α/β-phase region and the results showed that intensity of T-type texture is weakened dramatically and a single B-type texture is generated.[35] In general, at ambient temperature, the basal/pyramidal $\langle a \rangle$ slip, pyramidal $\langle c + a \rangle$ slip, and $\{10\bar{1}2\}$ twinning in titanium alloys all cause $\langle 001 \rangle$ direction shift to the applied loading direction, leading to the formation of B-type texture.[35,36] However, due to the interaction of β/α phases and DRX, the texture evolution mechanism in the two-phase region differs from that of room temperature deformation. As a result, it is important to reveal the texture evolution and its mechanism during two-phases cross rolling in titanium alloy.

In this study, microstructure and texture evolution and corresponding mechanical properties of the widely used Ti6Al4V alloy with initial lamellar structure after cross rolling in the α/β two-phase region were investigated. The DRX behavior and the evolution of B-type texture were analyzed as well. In addition, the correlation between B-type texture and tensile properties isotropy was discussed. The results could provide guidelines for producing isotropic ultrafine grain titanium alloy plate.

II. EXPERIMENTAL

In this experiment, traditional hot rolled 10 mm Ti6Al4V plates were used as the initial material. The measured composition of the alloy is given in Table I. The plates were then β quenched to obtain a fine lamellar α' structure, as shown in Figure 1. The texture of the as quenched sample (before cross rolling) is measured in Figure 2. Subsequently, the plates were heated to β/α phase region and cross pack rolled to 3.3 mm with reduction above 70 pct by one pass low temperature (β/α phase region as well, 750 °C–850 °C) cross pack rolling. Then the plates were cross rolled to 1 mm at a lower temperature by one pass. Before each rolling process, a 90 deg rotation along ND to the previous rolling direction is performed (i.e., cross rolling), which were labeled as CR1 and CR2, respectively. After that, CR1 and CR2 samples were annealed at different temperatures, respectively. The schematic illustration of the rolling and heat-treatment process is shown in Figure 3. Because the content of β phase is too small (< 10 pct), this paper mainly analyzes and discusses the α phase.

Tensile tests were performed on the annealed CR2 samples along both transverse and longitudinal direction under the requirement of GB/T228.1. The gauge length for tensile specimens is 24 mm. For as rolled and annealed samples, microstructures were observed on RD-TD plane. Microstructures were characterized by Gemini SEM300 field emission gun scanning electron

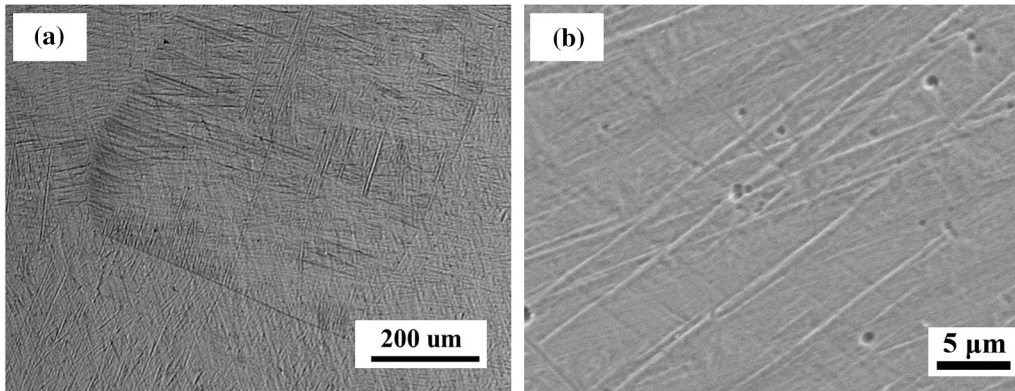|	C	O	N	H	Fe	Al	V	Ti
Ti-64 plate	< 0.01	0.13	< 0.01	0.001	0.15	6.22	4.15	balance

Fig. 1—Microstructure of the β quenched Ti6Al4V plate: (a) morphology of fine lamella α' phase in β grains; (b) close-up image of the fine lamella α' phase.
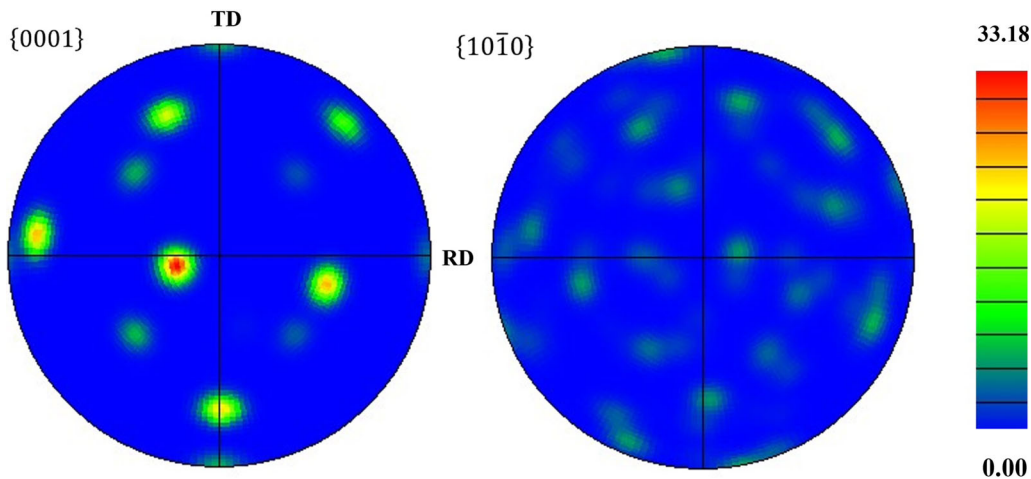

Fig. 2—Original texture of plate after β quenching.

microscope (SEM) with a high-resolution EBSD detector and Zeiss optical microscope and JEOL JEM-2100 F transmission electron microscopy (TEM). The scanning step size is 0.04 μm. Metallographic samples were ground with 240# to 3000# grit silicon carbide (SiC) metallographic sandpaper, followed by mechanical polishing and etching with Kroll solution. EBSD samples were ground with metallographic 3000# sandpaper and electrolytically polished using a mix of CH_3COOH: $HClO_4$ = 9:1. The polishing duration is ~ 30 seconds with voltage of and 36.5 V and current of 650 mA selected. Grain sizes of samples were determined using Image-J software.

A grain is defined as "subgrain" with an average misorientation angle between 2 and 7.5 deg. If the average misorientation angle within the grain exceeds 7.5 deg, the grain is classified as being "deformed". The remaining grains are classified as "recrystallized". The ranges of low angle grain boundaries (LAGBs) and high angle grain boundaries (HAGBs) are 2–15 deg and more than 15 deg, respectively.

III. RESULTS

A. Microstructure Evolution During Hot Cross Rolling

The microstructure of CR1 and CR2 sample is shown in Figure 4. As is shown in Figures 4(a) and (b), the microstructure and orientation distribution of the CR1 sample are displayed. After low temperature hot rolling of the β quenched plate, it is clearly seen that the size and morphology of the grain are not uniform. Both

coarse elongated grains and fine equiaxed grains are distributed. The coarse elongated grains are more likely oriented along ⟨001⟩/ND which is hard orientation in α phase. These hard oriented grains probably did not deform sufficiently to ensure DRX, while grow up during hot cross rolling process. The orientation of the fine equiaxed grain is more random, indicating that it was DRXed grains. Figure 4(c) shows the grain orientation spread (GOS) maps of CR1. DRXed grains (GOS < 2 deg, marked in blue), substructed (2 deg < GOS < 7.5 deg) and deformed grains (GOS > 7.5 deg) were distinguished by the GOS map.[37–39] The fine equiaxed grains appear typical discontinuous DRX (DDRX) characteristics, which are mostly distributed along the original grain boundaries. A large number of deformed grains and a small number of recrystallized areas exist in CR1 sample. Figures 4(d) and (e) show the microstructure of the CR2 plate. After the second cross rolling, the original coarse α lamellar were almost broken, and the microstructure of CR2 plate consisted of both micro-scaled equiaxed grains and some

submicro-scaled recrystallized grains. The average grain size is ~ 1.24 μm which suggesting that twice cross rolling could effectively refine the original lamella structure. However, the size distribution of the grain is still heterogeneous. Compared with CR1 sample, CR2 sample has an increased fraction of deformed grains, but the fraction of recrystallized grains is close to that of CR1. This stems from the lower rolling temperature and smaller height reductions inhibiting the occurrence of DRX. TEM bright field images of initial quenched samples, CR1 and CR2 samples are shown in Figures 5(a) through (c). The yellow arrow refers to the fine α′ lamella in the initial β quenched samples. While, white arrow refers to DRXed grains in the CR1 and CR2 samples. The selective area electron diffraction (SAED) patten of the CR1 and CR2 samples are inserted as well. Similar to which observed by EBSD, fine equiaxed grains are displayed in both CR1 and CR2 sample. In addition, both bright field images and the corresponding SAED images show that grain size of CR2 sample is finer than that of CR1.
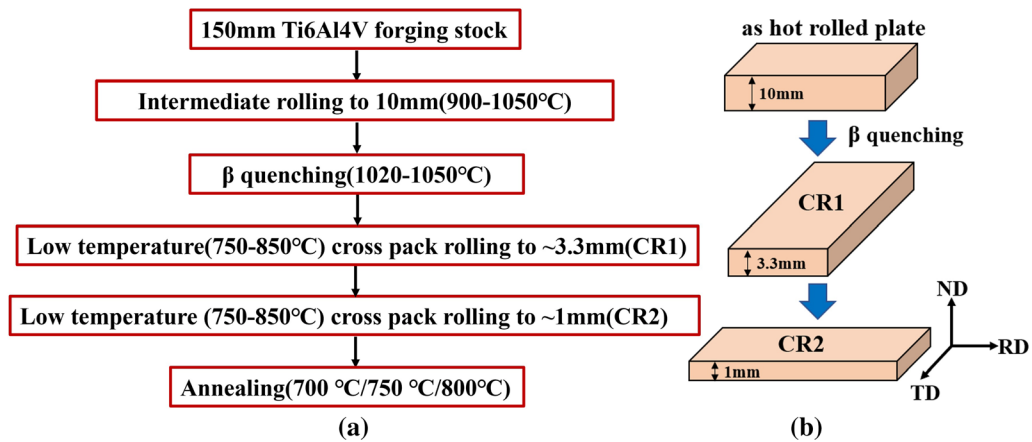

Fig. 3—(a) Illustration of hot cross rolling and heat-treatment process (b) Schematic figure of cross rolling process.
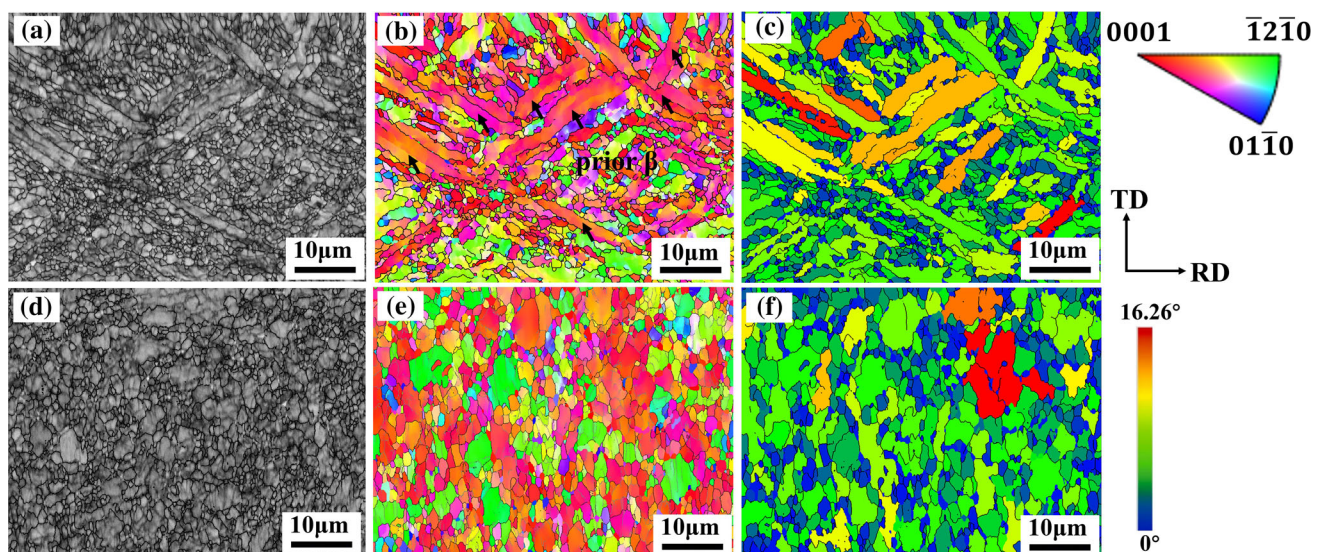

Fig. 4—The microstructure of CR1 (a) through (c) and CR2 (d) through (f). (a, d) band contrast maps, (b, e) IPF maps, (c, f) GOS maps.
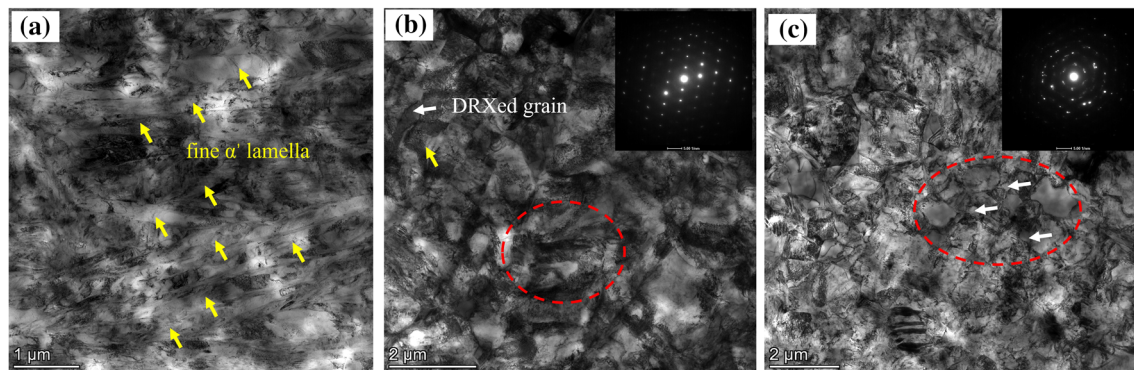
Fig. 5—TEM bright field images of quenched and cross rolling Ti6Al4V alloy: (a) fine lamella α' in β quenched sample; (b) DRXed grains in CR1 sample (c) DRXed grains in CR2 sample which displays finer grain size.
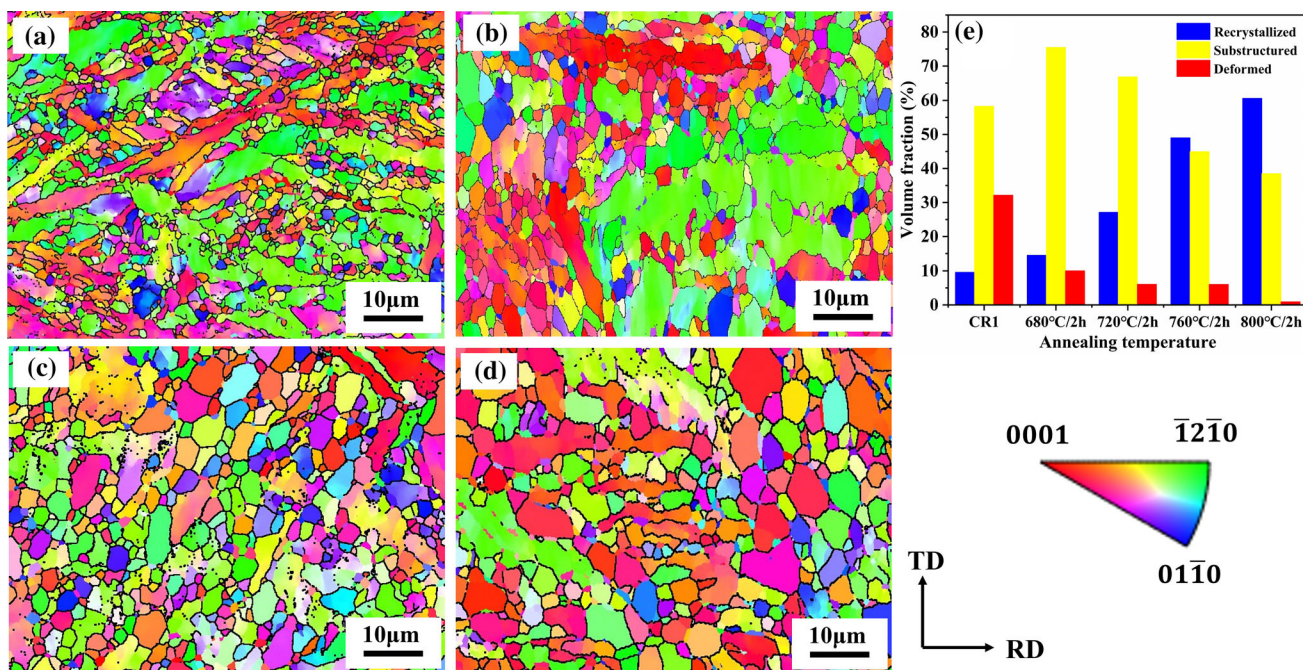

Fig. 6—IPF maps of CR1 sample annealed for 2 h at different temperature: (a) 680 °C (b) 720 °C (c) 760 °C and (d) 800 °C. The volume fraction of recrystallized, substructured and deformed region are listed in (e).

B. Microstructure Evolution During Annealing Treatment

Figure 6 shows the microstructure evolution of CR1 samples at different annealing temperatures. The microstructure after annealing at 680 °C is similar to that of the original rolled sample, consisting of a few elongated grains and equiaxed grains (Figure 6(a)). Meanwhile, as shown in Figure 6(e), the volume fraction of deformed microstructure is significantly reduced after annealing and replaced by a large number of substructure and recrystallized microstructure. As the annealing temperature increases, the recrystallization fraction increases significantly and the deformed fraction decreases. After annealing at 800 °C, the microstructure is almost composed of equiaxed grains and the recrystallization fraction reaches a maximum of 61 pct. To determine the effect of annealing time on

recrystallization, CR1 sample was annealed at 800 °C for different times and the corresponding IPF maps are shown in Figure 7. After short time (5 minutes) annealing, the fraction of recrystallized grains increased while the deformed grains decreased, indicating that static recovery (SRV) and static recrystallization (SRX) occurred during annealing. After annealing for 30 minutes, the fraction of recrystallized grains increased and the deformed grains almost disappeared. Thus, it is clear that high annealing temperatures and long annealing times tend to promote the SRV and SRX.

Figure 8 shows the IPF and recrystallization of CR2 sample annealed at different temperatures. After annealing at 700 °C, owing to the lower temperature, fraction of recrystallized grains increases slightly while the substructure fraction increased significantly compared to the hot rolled samples (Figure 8(d)). Spheroidization
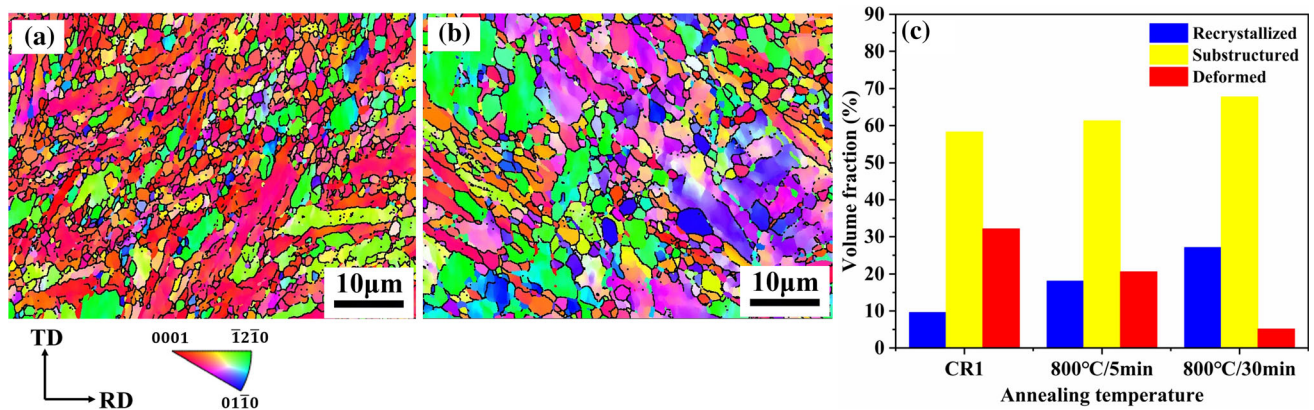
Fig. 7—IPF maps of CR1 sample annealed at 800 °C for different time: (*a*) 5 min and (*b*) 30 min. The volume fraction of recrystallized, substructured and deformed region are listed in (*c*).
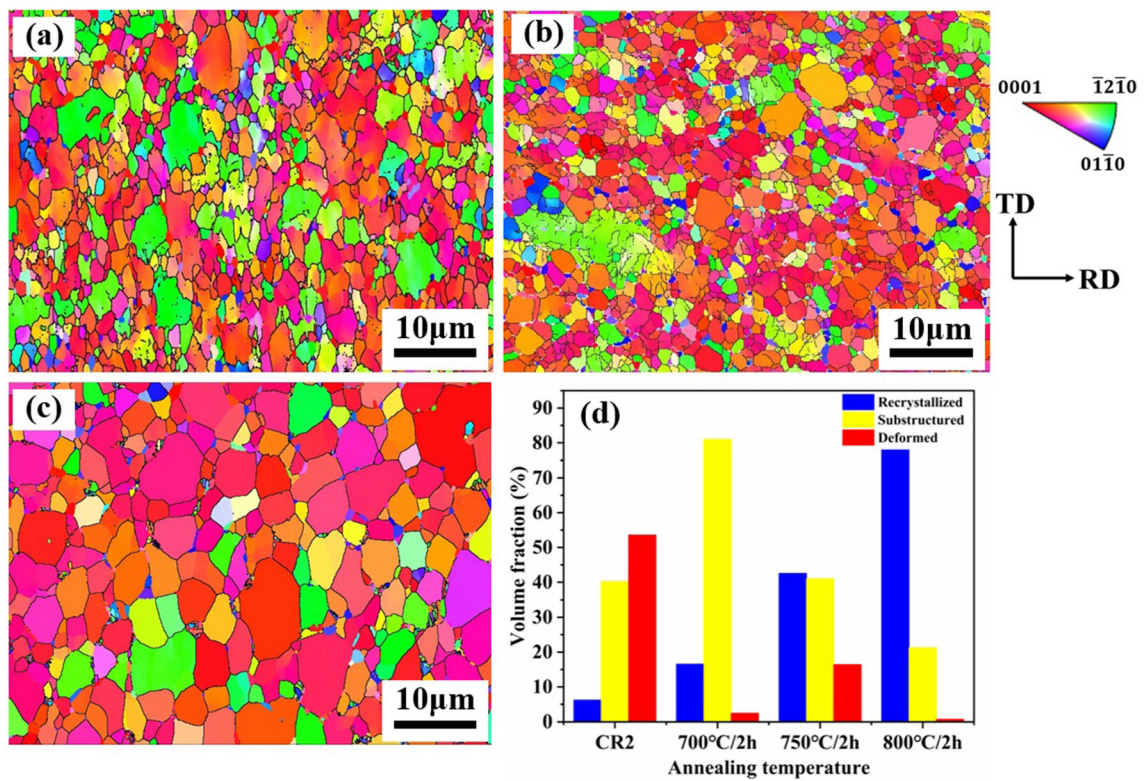

Fig. 8—IPF maps of CR2 sample annealed for 2 h at (*a*) 700 °C (*b*) 750 °C and (*c*) 800 °C. The volume fraction of recrystallized, substructured and deformed region are listed in (*d*).

of the grains caused by SRX leads to a refined grain with average size ~ 1.3 μm. At 750 °C and 800 °C (Figures 8(b) and (c)), more fraction of grains recrystallizes accompanying grain growth. The average grain size increases to 1.4 and 2.5 μm. In addition, as shown in Figures 4 and 8, the grain size difference after annealing especially high temperature annealing is reduced obviously. The obvious difference in grain size after CR1 probably on account of the different local strain distribution which results in different extent of DRX.

In grains with soft orientation ([11$\bar{2}$0]//ND, [10$\bar{1}$0]//ND), higher strain is accumulated which promotes the nucleation and growth of recrystallized grains. However, in grains with hard orientation ([0001]//ND), local strain is not high enough to generate DRX. The DRV is more likely to occur which retains the elongated initial grain instead of grain refinement. Finally, a mixed microstructure with small recrystallized grains and coarse non-recrystallized grains is displayed in the rolled samples. As the annealing temperature increases, grain
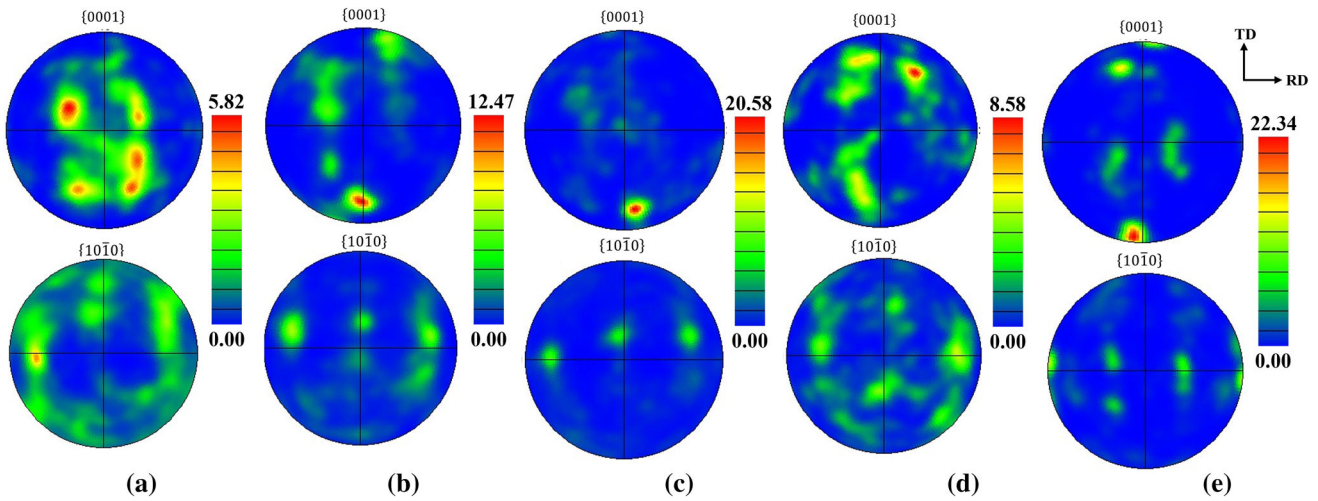
Fig. 9—Texture evolution of CR1 sample: (*a*) as cross rolled (*b*) 680 °C annealed (*c*) 720 °C annealed (*d*) 760 °C annealed and (*e*) 840 °C annealed.
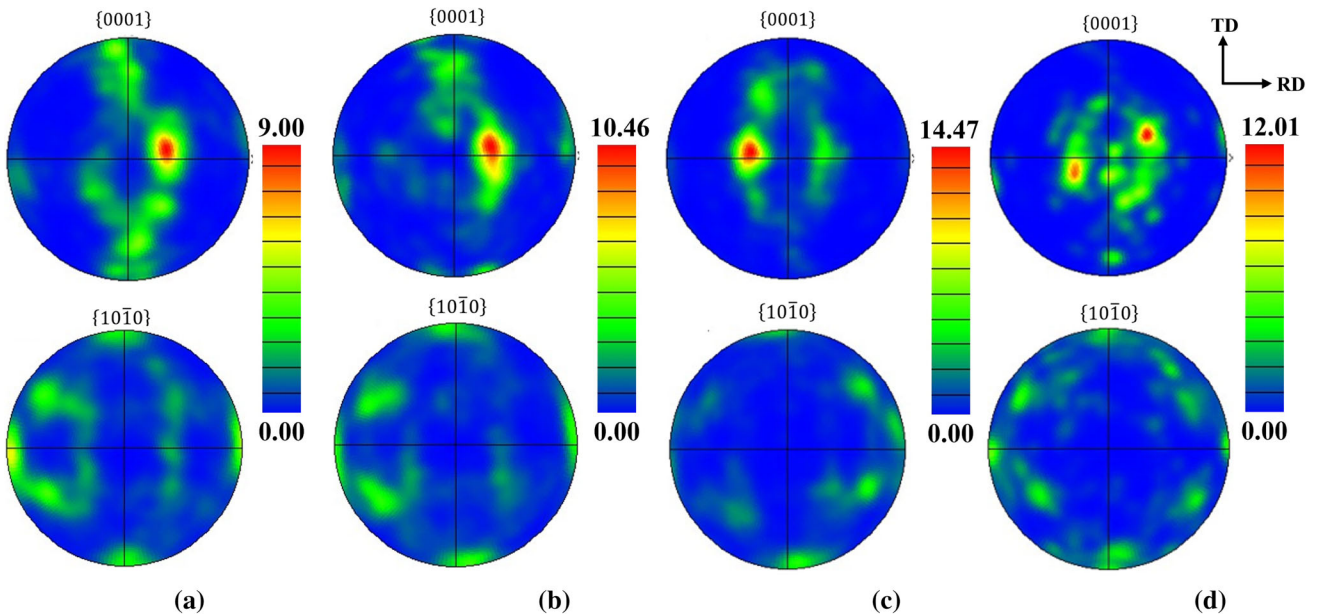

Fig. 10—Texture evolution of CR2 sample (*a*) as cross rolled (*b*) 700 °C annealed (*c*) 750 °C annealed and (*d*) 800 °C annealed.

boundary migration becomes more active. The pre-re-crystallized grains are growing continually at the expense of small grains, which finally leads to a more uniform size distribution with higher grain size.

C. *Texture Evolution During Hot Cross Rolling and Subsequent Annealing*

Figure 9 shows the pole figure of CR1 samples before and after annealing at different temperatures. After first hot cross rolling (Figure 9(a)), the grain orientation tends to rotate to [0001]//ND direction. The maximum intensity is located about 26 deg inclination along ND

toward RD in (0001) pole figure. After annealing, the texture is transformed to a T-type texture ([0001]//TD) regardless of the annealing temperatures. Figure 10 shows the pole figure of CR2 samples before and after annealing at different temperatures. As seen in Figure 10(a), the overall orientation of CR2 sample is mainly located in TD-ND plane with a maximum intensity near ND. Compared to CR1 sample, CR2 sample displays (Figure 10(a)) a more concentrated basal texture (0001//ND) and a lower component of T-type texture (0001//TD). In addition, regardless of the annealing temperature, the annealing texture is close to that of the hot rolling one, both of which are mainly
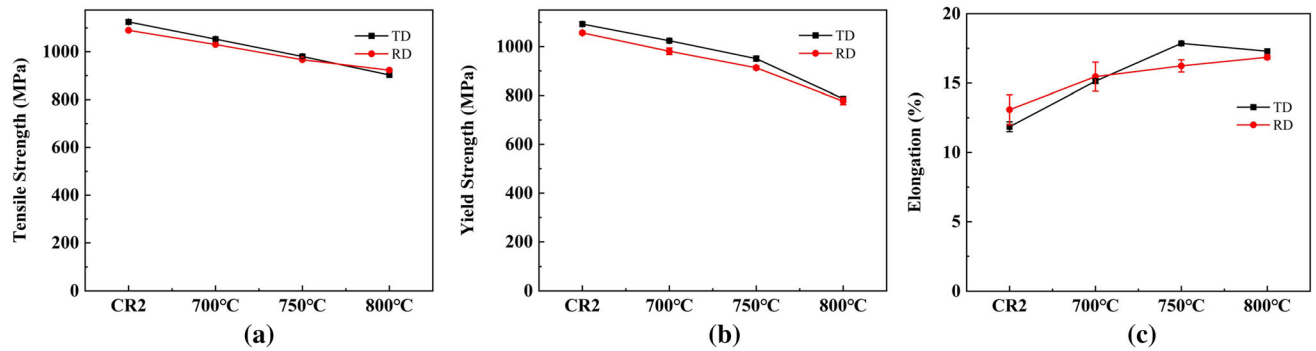
Fig.11—CR2 Tensile properties of CR2 sample after annealing at different temperature: (*a*) tensile strength, (*b*) yield strength, (*c*) elongation at fracture.
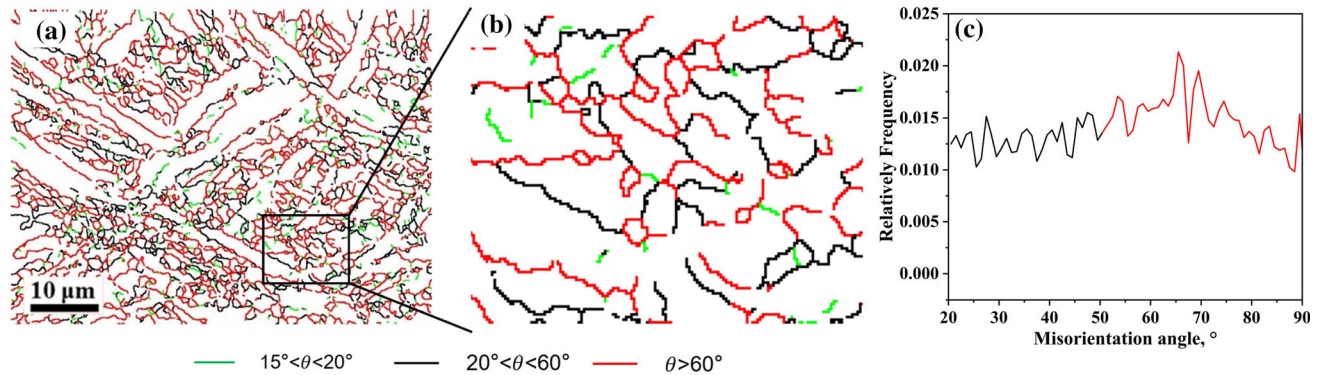

Fig. 12—HAGBs distribution of CR1 sample: (*a*) overall grain boundary diagram (*b*) close-up image of (*a*), (*c*) misorientation angle distribution of medium range (20–50 deg), and very high range (> 50 deg) for HAGBs.

consist of basal texture component ([0001]//ND). The intensity of [0001]//TD orientation gradually decreases as annealing temperature increasing. In general, it is clearly seen that after twice cross rolling, the [0001] direction in most grains is aligned with ND (*i.e.,* forming a B-type texture). Annealing of CR2 sample does not change the texture type but increase the intensity slightly. In the (10 $\bar{1}$ 0) pole figure, a weak component of [10 $\bar{1}$ 0]//RD texture is displayed.

D. *Tensile Properties of the CR2 Sample*

The room temperature tensile properties of CR2 sample before and after annealing at different temperatures are shown in Figure 11. It is obvious that cross rolled sample exhibits advanced strength-ductility combination. The tensile strength, yield strength and elongation at fracture of the as cross rolled sample are 1090.03 MPa, 1056.31 MPa,13.08 pct along RD and 1125.18 MPa, 1092.39 MPa, 11.85 pct along TD, respectively. Meanwhile, the strength decreases with the increase of annealing temperature. Tensile strength and yield strength decrease to 922.49 MPa and 776.91 MPa in RD sample, and 902.60 MPa and 786.79 MPa in TD sample as annealing temperature increasing to 800 °C. In addition, it is clearly seen from

Figures 11(a) and (b) that the strength in TD is slightly higher than that in RD. As annealing temperature increases, the strength difference between TD and RD gradually decreases. Meanwhile, elongation of both TD and RD sample is increasing with incremental annealing temperature.

IV. DISCUSSION

A. *Recrystallization During Hot Cross Rolling and Annealing Process*

1. *DRX behavior during hot cross rolling*

During cross rolling, relative high temperature and large reduction lead to the emergence of DRX. In the IPF map of CR1 sample (Figure 4(b)), it is observed that fine equiaxed grains are mainly distributed along the original grain boundaries, and a "necklace structure" appears in some regions, which is typical feature of the occurrence of discontinuous DRX (DDRX).[25,40] Generally speaking, the formation of DDRXed grains was the result of HAGBs migration. While the grain misorientation angle of continuous DRX (CDRX) is transformed from LAGBs to HAGBs. Hence, DDRXed grains have random misorientation angle grain boundaries, in which there will be also very high angle
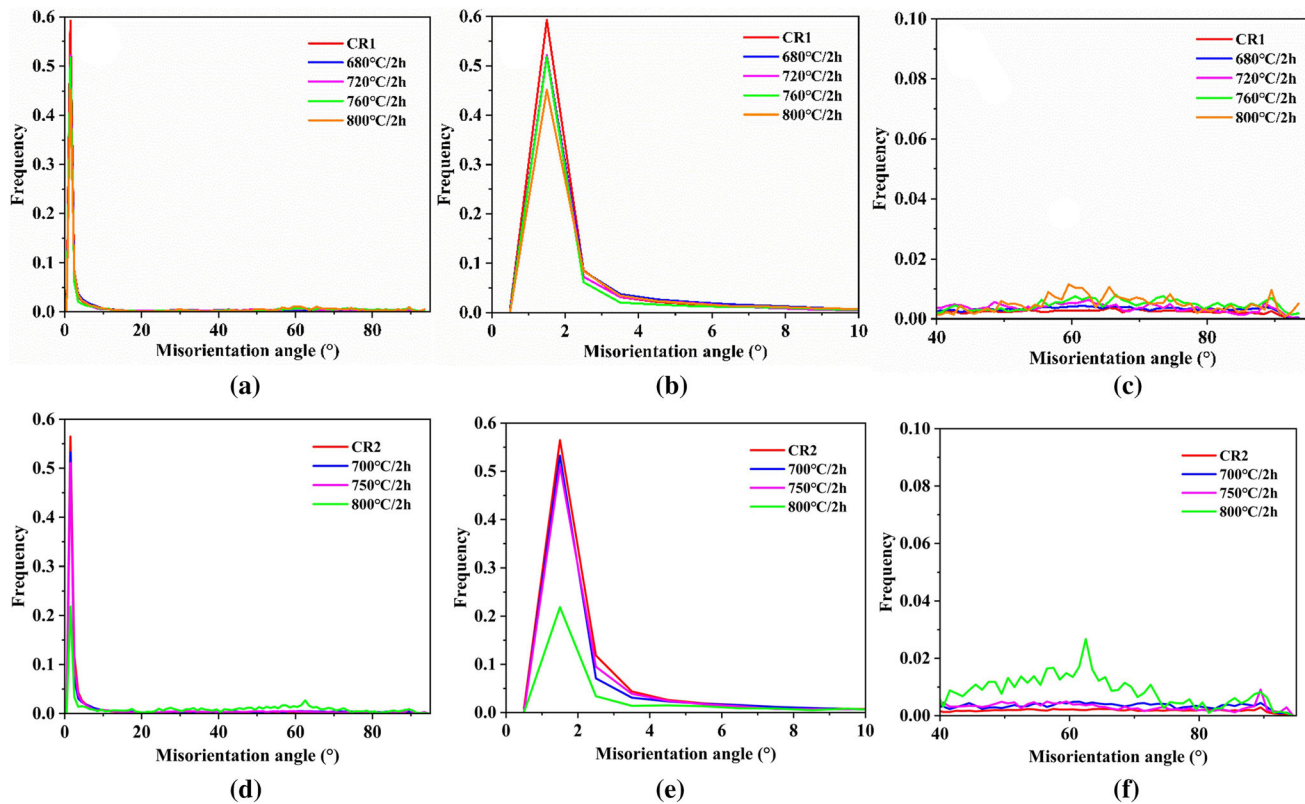
Fig. 13—Distribution of grain boundary misorientation of CR1 and CR2 sample after annealing at different temperature: (*a*) and (*d*) over misorientation of CR1and CR2 sample, (*b*) and (*e*) close-up image of misorientation angle bellow 10 deg, (*c*) and (*f*) close-up image of misorientation between 40 and 90 deg.

boundaries. In contrast, the newly formed CDRXed grains will have HAGBs (from the LAGBs) close to 15 deg and of a "not so high" misorientation.[40] As seen in Figure 12(a), the misorientation angles of grain boundary in CR1 sample are divided into low range (15–20 deg), medium range (20–50 deg), and very high range (> 50 deg) for HAGBs. The results show that most of the DRXed grains have grain boundary misorientation angle located in the middle range and very high range, where grains with HAGBs in the low range (15–20 deg) may be generated by CDRX or DDRX mechanism. However, grains completely surrounded by HAGBs (> 20 deg) are not possible to be generated due to CDRX mechanism (Figure 12(b)). The evolution of the distribution of HAGBs is shown in Figure 12(c). Proportion of HAGBs with misorientation angle > 60 deg is higher than that of with low misorientation angle (15–20 deg). Therefore, it is reasonable to consider that CR1 sample mainly underwent DDRX during hot cross rolling. The occurrence of DDRX forms new equiaxed grains which is beneficial for grain refinement. At the same time, the formation of fine equiaxed grains were also related to the rolling

temperature. Relative low temperature rolling in two-phase region ensures the recrystallization process while inhibits the grain growth. As seen in Figure 4(b), it is worth mentioning that a part of coarse grains with [0001]//ND orientation. The [0001] oriented grains are hard orientation, which will not exhibit sufficient plastic strain to initiate the DRX process.

B. SRX Behavior During Annealing

The gradual globularization of α grains takes place with increasing annealing temperature which is due to the SRX. To further determine the type of SRX, the distribution of grain boundary misorientation angle of CR1 and CR2 sample after annealing at different temperatures is shown in Figure 13. As in CR1 sample, it is clearly seen that fraction of LAGBs (< 10 deg) is dominant while fraction of HAGBs is relatively low in both cross rolling and annealing treatment (Figures 13(a) through (c)). In addition, as seen in Figures 11(c) and 13(b), it is worth noting that the fraction of LAGBs decreases while the fraction of HAGBs increases with incremental annealing

temperature, which indicates that the HAGBs are formed by the gradual increase of the misorientation angle of the LAGBs. This transition is a significant feature of the microstructure undergoing continuous SRX (CSRX) (see Figures 13(d) through (f)).[26] During the CSRX, LAGBs absorb dislocations to transform into HAGBs, which prompts the substructure grain to transformed into recrystallized grains. The increase of annealing temperature decreases the lattice resistance for dislocation movement, which promotes the nucleation of substructures and the absorption of dislocations, in turn promoting the occurrence of CSRX. In addition, the annealing process of CR2 sample was similar to that of CR1 sample. With increasing annealing temperature, LAGBs gradually transform into HAGBs *i.e.,* CSRX takes place (Figures 13(d) through (f)).

C. *Texture Evolution During Cross Rolling and Annealing*

To analyze texture evolution during cross rolling and annealing, the texture of the as quenched sample (before cross rolling) was measured (Figure 2). In general, a more random grain orientation is displayed. After first cross rolling, the dispersive B-type texture was observed with maximum intensity located at the position of 26 deg inclination from RD to TD (Figure 9(a)). After the second cross rolling, maximum intensity was located along ND tilted about 26° toward RD, basically forming a B-type texture. It has been shown[41] that different c/a ratios lead to the activation of different slip systems, resulting in different types of deformation textures. For Ti with c/a ratio less than 1.633 (1.587), prismatic and basal $\langle a \rangle$ slip system lead to the formation of [0001] direction tilted $\pm$ 20–40 deg from ND to TD, and (10$\bar{1}$0)//RD deformation textures.[41] Li *et al.*[35] found that in α/β two-phase region rolling, prismatic $\langle a \rangle$ slip and basal $\langle a \rangle$ slip system facilitate the formation of for T-type and B-type texture, respectively. Meanwhile, texture simulation computed by CPFEM suggested that both pyramidal $\langle a \rangle$ and $\langle a + c \rangle$ slip facilitate the rotation of $\langle 001 \rangle$ direction towards ND.[42] As shown in Figures 15(d) and (e), the average Schmid factors along ND direction are 0.252 and 0.358 for the prismatic and basal $\langle a \rangle$ slip system in CR2 sample. Obviously, basal $\langle a \rangle$ slip system displays a much higher Schmid factor along ND direction which promotes the formation of B-type texture. Therefore, after the second cross rolling, the CR2 sample basically formed B-type texture. In addition, basal poles are located at an inclination of about 25 deg from ND to RD (Figure 10(a)). This orientation is attributed to both the compressive stress along ND and the friction-induced shear stress along RD during rolling process.

D. *Analysis of Microstructure-Tension Property Correlation*

1. *Effect of annealing temperature on mechanical properties*

As clearly seen in Figure 11, both tensile strength and yield strength are decreasing with incremental annealing temperature. The well-known Hall–Petch law is used to illustrate the relationship between grain size and strength.[43]

$$\sigma_s = \sigma_0 + Kd^{-\frac{1}{2}} \tag{1}$$

With the increase of annealing temperature, the grain size d increases and yield strength gradually decrease, which are basically in accordance with the Hall–Petch relationship. In addition, during the subsequent annealing, both SRV and SRX take place, the dislocation density decreases and the work-hardening effect disappears, resulting in the reduction of strength. The geometrically necessary dislocation density (GNDs) of CR2 samples at different annealing temperatures is shown in Figure 14. The GND density is calculated which based on the strain gradient theory, as shown in Eq. [2].[44,45]

$$\rho^{GND} = \frac{2\theta}{uB} \tag{2}$$

ρ^{GND} represents the GND density, θ is the local misorientation, u is the scanning step size for the EBSD map (0.04 μm), B is the Burgers vector (0.295 nm for α-Ti).[46] GNDs decreases with increasing annealing temperature. After annealing at 800 °C, the average GNDs of the specimens is 4.07×10^{14} m^{-2}, which is an order of magnitude lower compared to CR2 sample. According to the classical Taylor equation[47]:

$$\sigma_0 = M\alpha Gb\sqrt{\rho} \tag{3}$$

σ_0 is the alloy strength, G is the shear modulus, b is the Burgers vector, and α is Taylor factor. The strength is gradually decreased owing to the decrease of dislocation density with elevated annealing temperature.

E. *Effect of Texture on Mechanical Properties*

As shown in Figure 10, basal texture is mainly displayed in both rolled and annealed samples in CR2 samples. The strength difference between RD and TD is relatively limited (below 50 MPa). In order to determine the relationship between crystal orientation and strength, it is very significant to determine the deformation mode. The mainly deformation modes in *hcp* α phase are dislocation slip and twinning. Twinning plays an important role under low temperature and high strain rate.[48–51] In this paper, twinning is not detected. Therefore, only dislocation slip is discussed hereafter.
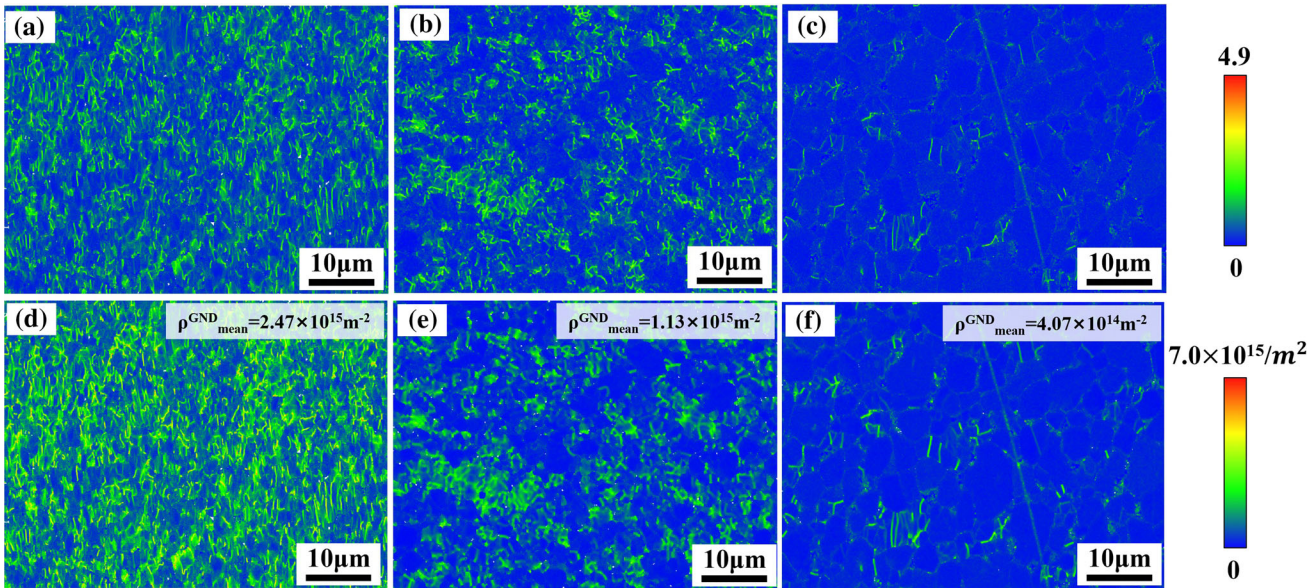
Fig. 14—KAM maps and GND maps of CR2 annealed samples (*a, d*) 700 °C (*b, e*) 750 °C (*c, f*) 800 °C.

The rolled and annealed CR2 specimens have a limited component of T texture, resulting in a higher strength in TD than RD (Figure 11). Figure 15 shows the Schmid factor distribution of different slip systems. The average SF values in RD and TD direction are relatively high which make the prismatic ⟨*a*⟩ slip system easy to be activated. Moreover, SF values in RD is the largest followed by TD, and the smallest is ND which suggested hat prismatic ⟨*a*⟩ slip system along RD is easiest to initiate, determining a lower yield strength comparing to TD direction. SF values for pyramidal ⟨*a*⟩ slip system after annealing at different temperatures is show in Figure 15(f) which also show a higher SF value of RD sample than TD sample. This indicates that pyramidal ⟨*a*⟩ slip system is easier to activated along RD. In addition, both prismatic and pyramidal SF values along TD is increased rapidly with incremental annealing temperature. This phenomenon could explain the decreasing strength difference between RD and TD sample during annealing. As seen in Figures 15(b) and (e), SF values of basal ⟨*a*⟩ slip system is much lower along TD and RD direction comparing to ND. This is reasonable to consider that basal ⟨*a*⟩ slip system is less likely to be activated. In summary, the prismatic and pyramidal ⟨*a*⟩ slip system were easily to be activated during tensile test. The SF values in RD sample was higher than that in TD, resulting prismatic and pyramidal ⟨*a*⟩ slip system easily activated along RD, furtherly leading to slightly lower yield strengths in RD sample. As the annealing temperature increases, SF values in TD gradually increases and the increasing rate is much larger than that in RD, resulting in a small strengths difference between TD and RD samples.

V. CONCLUSIONS

In this paper, the β quenched Ti6Al4V plates were cross rolling in α/β two-phase region and annealed at different temperatures. The microstructure evolution, texture variation and recrystallization behavior were characterized. Correlation between microstructure, texture and tensile strength were discussed. The main conclusions were as follows:

(1) After first cross rolling, partial DDRX takes place which results in a refined but inhomogeneous microstructure. During subsequent annealing, grain size distribution become more uniform owing to the CSRX and grain growth.

(2) After second cross rolling, the grain was refined to 1.24 μm. An equiaxed ultrafine grain could obtained during subsequent annealing treatment. The texture is transformed into a B-type ([0001]// ND) texture which results in a small strength difference between TD and RD sample.

(3) The RD sample displayed highest SF for prismatic ⟨*a*⟩ slip system which is the origin of the lower strength comparing to TD counterpart. With increasing annealing temperature, SF value difference of prismatic ⟨*a*⟩ slip system between RD and TD sample is decreasing which is beneficial to reduce anisotropy of Ti6Al4V plates.
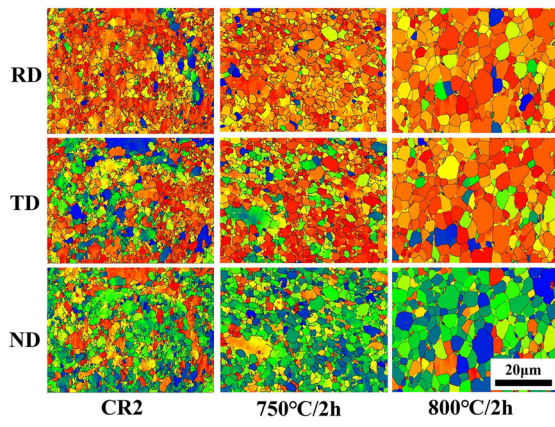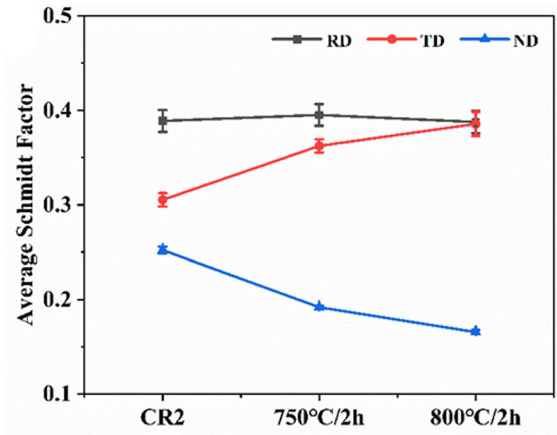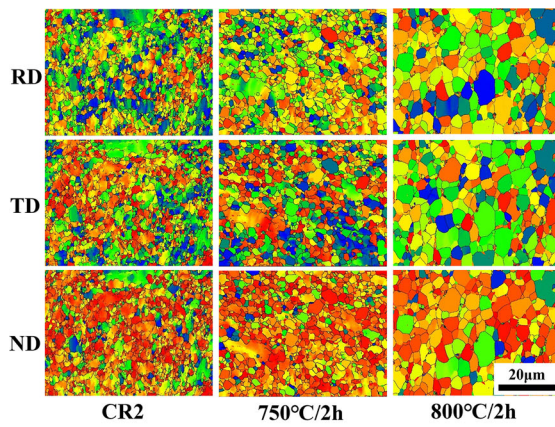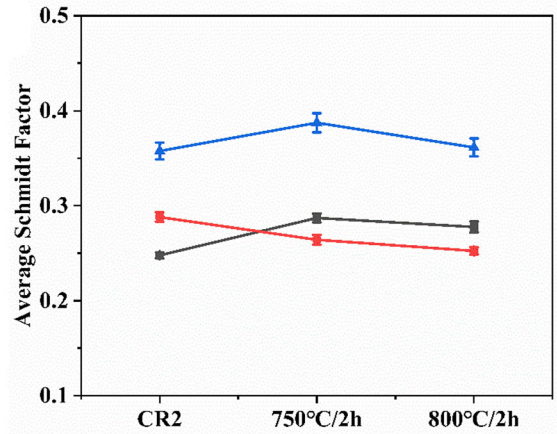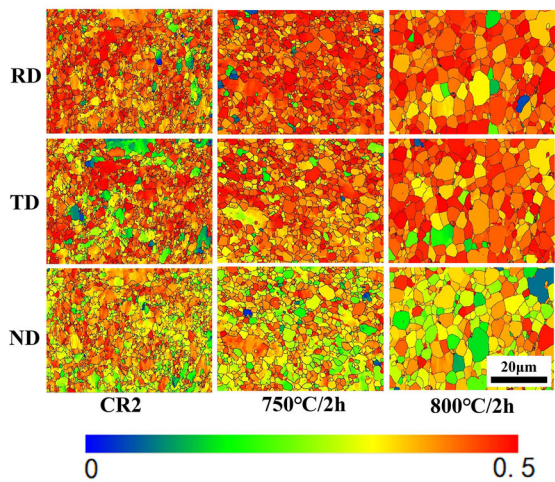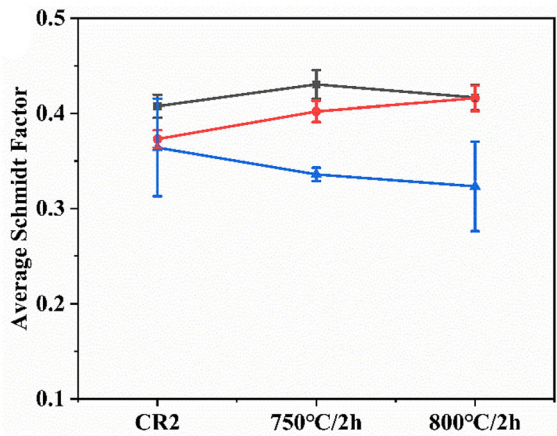
Fig. 15—SF values distribution for CR2 sample with different loading directions: (*a*) and (*d*) SF distribution map and average SF of prismatic ⟨*a*⟩ slip system; (*b*) and (*e*) SF distribution map and average SF of basal ⟨*a*⟩ slip; (*c*) and (*f*) SF distribution map and average SF of pyramidal ⟨*a*⟩ slip system.

ACKNOWLEDGMENTS

CONFLICT OF INTEREST

On behalf of all authors, the corresponding author states that there is no conflict of interest.

REFERENCES

1. O.M. Ivasishin, P.E. Markovsky, Y.V. Matviychuk, S.L. Semiatin, C.H. Ward, and S. Fox: *J. Alloys Compd.*, 2013, vol. 550, pp. 23–30.
2. C.L. Li, X.J. Mi, W.J. Ye, S.X. Hui, Y. Yang, and W.Q. Wang: *J. Alloys Compd.*, 2013, vol. 550, pp. 23–30.
3. S. Shekhar, R. Sarkar, S.K. Kar, and A. BhattacharjeeL: *Mater. Des.*, 2015, vol. 66, pp. 596–610.
4. J. Fan, J. Li, H. Kou, K. Hua, B. Tang, and Y.D. Zhang: *J. Alloys Compd.*, 2016, vol. 682, pp. 517–24.
5. J.W. Lu, Y.Q. Zhao, P. Ge, H.Z. Niu, Y.S. Zhang, W. Zhang, and P.X. Zhang: *Mater. Sci. Eng. A*, 2015, vol. 621, pp. 182–89.
6. X. Xu, G. Wang, and C. Xia: *Mater. Des.*, 2012, vol. 36, pp. 136–40.
7. Z. Zhang, L. Ming, D. Guo, Y. Shi, T. Ma, G. Zhang, and X. Zhang: *Mater. Sci. Eng. A*, 2013, vol. 588, pp. 416–19.
8. A. Medvedev, H.P. Ng, R. Lapovok, Y. Estrin, T.C. Lowe, and V.N. Anumalasetty: *Mater. Lett.*, 2015, vol. 145, pp. 308–11.
9. Q.J. Sun and X. Xie: *Mater. Sci. Eng. A*, 2018, vol. 724, pp. 493–501.
10. M. Ashida, P. Chen, H. Doi, Y. Tsutsumi, T. Hanawa, and Z. Horita: *Mater. Sci. Eng. A*, 2015, vol. 640, pp. 449–53.
11. G.H. Liu, T.R. Li, M. Xu, T.L. Fu, Y. Li, Z.D. Wang, and G.D. Wang: *Acta Metall. Sin.*, 2017, vol. 53, pp. 1038–46.
12. H.Z. Li, Y. Long, X.P. Liang, Y.X. Che, Z.Q. Liu, Y. Liu, H. Xu, and L. Wang: *Intermetallics*, 2020, vol. 116, 106647.
13. K. Ozbeyaz, H. Kaya, and A. Kentli: *Met. Mater. Int.*, 2022, vol. 28, pp. 1290–305.
14. S. Muralidharan and U.M. Iqbal: *Int. J. Mater. Form.*, 2023, vol. 16, p. 6.
15. B.O. Shahreza, J. Huot, M. Antonov, L. Kommel, F. Sergejev, F.J.P. Trujillo, A. Heczel, and J. Gubicza: *Int. J. Refract. Met. Hard Mat.*, 2023, vol. 111, 106079.
16. Y.H. Wei, L.W. Lu, M.H. Li, M. Ma, W.Y. Huang, X. Zhao, and R.Z. Wu: *J. Alloys Compd.*, 2023, vol. 948, 169720.
17. E.E. Klu, D. Song, C. Li, G. Wang, B. Gao, A. Ma, and J. Jiang: *Mater. Sci. Eng. A*, 2022, vol. 833, 142371.
18. A. Msr, A. Hm, A. Bjl, A. Hp, B. Mrt, and I. Sun: *Mater. Sci. Eng. A*, 2021, vol. 824, 141803.
19. B. Hu, B.B. He, G.J. Cheng, H.W. Yen, M.X. Huang, and H.W. Luo: *Acta Mater.*, 2019, vol. 174, pp. 131–41.
20. X.J. Shen, S. Tang, G.D. Wang, Q.Y. Zhang, and X.N. Wang: *J. Manuf. Process.*, 2021, vol. 70, pp. 321–30.
21. T. Inoue and R. Ueji: *Mater. Sci. Eng. A*, 2020, vol. 786, 139415.
22. J. Hu, L.X. Du, H. Xie, P. Yu, and R.D.K. Misra: *Mater. Sci. Eng. A*, 2014, vol. 605, pp. 186–91.
23. C.H. Park, J.H. Kim, J.-T. Yeom, C.-S. Oh, S.L. Semiatin, and C.S. Lee: *Scr. Mater.*, 2013, vol. 68, pp. 996–99.
24. H. Liang, H. Guo, Y. Ning, X. Peng, C. Qin, Z. Shi, and Y. Nan: *Mater. Des.*, 2014, vol. 63, pp. 798–804.
25. D. He, J.C. Zhu, Z.H. Lai, Y. Liu, and X.W. Yang: *Mater. Des.*, 2013, vol. 46, pp. 38–48.
26. K. Wang, M. Wu, Z. Yan, D. Li, R. Xin, and Q. Liu: *Mater. Sci. Eng. A*, 2018, vol. 712, pp. 440–52.
27. H. Matsumoto, L. Bin, S.H. Lee, Y.P. Li, Y. Ono, and A. Chiba: *Metall. Mater. Trans. A*, 2013, vol. 44, pp. 3245–260.
28. L.P. Xin, K. Wang, Z.B. Yan, D.R. Li, R.L. Xin, and Q. Liu: *Materialwiss. Werkstofftech.*, 2019, vol. 50, pp. 1545–554.
29. E.T. Burkhart, and L. Hefti: *SAE International Journal of Advances and Current Practices in Mobility*, 2020, vol. 2, pp. 1202–1208.
30. Z. Hu, Z. Chen, J. Xiong, T. Chen, J. Shao, and C. Liu: *Mater. Sci. Eng. A*, 2016, vol. 662, pp. 519–27.
31. L.L.C. Catorceno, H.F.G. de Abreu, and A.F. Padilha: *J. Magnes. Alloys*, 2018, vol. 6, pp. 121–33.
32. Z.G. Li, L. Chen, J.W. Tang, W.C. Sun, G.Q. Zhao, and C.S. Zhang: *J. Alloys Compd.*, 2021, vol. 863, 158725.
33. D.K. Liu, G.S. Huang, G.L. Gong, G.G. Wang, and F.S. Pan: *Trans. Nonferrous Met. Soc. China*, 2017, vol. 27, pp. 1306–312.
34. A. Gupta, R.K. Khatirkar, T. Dandekar, and D. Mahadule: *J. Alloys Compd.*, 2020, vol. 850, 156824.
35. W.Y. Li, Z.Y. Chen, J.R. Liu, S.X. Zhu, G.X. Sui, and Q.J. Wang: *J. Mater. Sci. Technol.*, 2019, vol. 35, pp. 790–98.
36. J.J.W. Won, D. Kim, S.G. Hong, and C.S. Lee: *J. Alloys Compd.*, 2016, vol. 683, pp. 92–99.
37. L. Zhang, S. Yuan, J.H. Wang, L.J. Chen, and P.P. Jin: *J. Alloys Compd.*, 2022, vol. 922, 166244.
38. X. Zhang, Z.G. Luo, G.G. Xie, H. Yu, Z.S. Liu, and J.S. Yang: *Mater. Sci. Eng. A*, 2022, vol. 850, 143582.
39. S. Dixit, D. Kumar, B.B. Dash, S. Suwas, A. Bhattacharjee, and S. Sankaran: *J. Alloys Compd.*, 2022, vol. 927, 166897.
40. R. Kapoor, G.B. Reddy, and A. Sarkar: *Mater. Sci. Eng. A*, 2018, vol. 718, pp. 104–10.
41. Y.N. Wang and J.C. Huang: *Mater. Chem. Phys.*, 2003, vol. 81, pp. 11–26.
42. A. Chapuis and Q. Liu: *Comput. Mater. Sci.*, 2015, vol. 97, pp. 121–26.
43. E.O. Hall: *Proc. Phys. Soc. Sect. B*, 1951, vol. 64, pp. 747–53.
44. H. Gao: *J. Mech. Phys. Solids*, 1999, vol. 47, pp. 1239–263.
45. L.P. Kubin and A. Mortensen: *Scr. Mater.*, 2003, vol. 48, pp. 119–25.
46. Y.F. Zheng, R.E.A. Williams, G.B. Viswanathan, W.A.T. Clark, and H.L. Fraser: *Acta Mater.*, 2018, vol. 150, pp. 25–39.
47. K. Ma, H. Wen, T. Hu, T.D. Topping, D. Isheim, D.N. Seidman, E.J. Lavernia, and J.M. Schoenung: *Acta Mater.*, 2014, vol. 62, pp. 141–55.
48. B.X. Zhou, R. Yang, B.S. Wang, L.P. Deng, and Y.H. Zhang: *Mater. Sci. Eng. A*, 2021, vol. 803, 140458.
49. Z.W. Yan, L. Wang, X.F. Xu, Z. Zhou, A.J. Liu, and Z.X. Ning: *Mater. Sci. Technol.*, 2022, vol. 38, pp. 1037–45.
50. E. Wielewski, C.R. Siviour, and N. Petrinic: *Scr. Mater.*, 2012, vol. 67, pp. 229–32.
51. J.W. Won, K.T. Park, S.G. Hong, and C.S. Lee: *Mater. Sci. Eng. A*, 2015, vol. 637, pp. 215–21.